Tracking the Cortico-Spinal Tract as a Multi-Modal Distribution of Streamlines from Local White Matter Microstructure Models

Aymeric Stamm, Olivier Commowick, Xavier Tomas-Fernandez, Jolene Singh, Simon K. Warfield

Tracking the Cortico-Spinal Tract as a Multi-Modal Distribution of Streamlines from Local White Matter Microstructure Models

Aymeric Stamm[1], Olivier Commowick[2], Xavier Tomas-Fernandez[1], Jolene M. Singh[1], and Simon K. Warfield[1]

[1] Computational Radiology Laboratory, Boston Children's Hospital, Boston MA USA
[2] VISAGES: INSERM U746 - CNRS UMR6074 - INRIA - Univ. of Rennes I, France
Contact: aymeric.stamm@childrens.harvard.edu

Abstract. We present a pipeline to reconstruct the corticospinal tract (CST) that connects the spinal cord to the motor cortex. The proposed method combines a new white matter microstructure model coined Diffusion Directions Imaging and a new tractography algorithm based on a particle filter adapted for approximating multi-modal distributions. In this paper, we put the computation time and accuracy of our pipeline to the test in the context of the MICCAI 2014 DTI challenge, which aims to provide fast and accurate reconstructions of the CST for presurgical planning of brain tumor extraction. These two key performance metrics are expected in such a situation where time is of the essence and the quality of the data is dependent on the patient's health condition and ability to cooperate. In no more than 1.5 hours per patient, we successfully provide accurate CSTs of 2 very collaborative patients who underwent a diffusion MRI protocol that included 69 diffusion-sensitizing gradients spread over 4 different shells ranging from $b = 200$ to $b = 3000$ s/mm^2.

1 Introduction

Diffusion-weighted (DW) MRI offers a unique way to explore *in-vivo* and *non-invasively* the functional architecture of the brain [1]. One of its prominent applications pertains to the inference of axonal wiring in the white matter (WM), where neuronal information transits [2]. Major axonal pathways, termed **fascicles**, are responsible for proper functional activity (e.g., language, vision, consciousness). Among these fascicles, the corticospinal tract (CST) connects the spinal cord and the motor cortex and governs our overall motor ability.

Providing an accurate reconstruction (composition and architecture) of the CST would be invaluable to the neurosurgeon in presurgical planning (e.g. brain tumor extraction), as it could facilitate and improve decision-making for better preserving motor functions after successful surgery. However, this reconstruction is most challenging. First, the CST goes through intricate anatomical regions, such as the semioval centrum, which are the crossroads of multiple fascicles. For instance, the CST crosses with the projections from the corpus callosum

and with the superior longitudinal fasciculus. Secondly, the CST architecture is quite complex on its own. While all CST axons are regrouped at the decussation of the superior cerebellar peduncle, they connect to the whole primary motor cortex extending anteriorly from the central sulcus (e.g., feet area), which is mainly a straight path, to the precentral sulcus (e.g., lip and tongue areas), which requires axonal bendings to be reached [3].

State of the art on WM fascicle reconstruction suggests that both an accurate model of the white matter microstructure and a probabilistic way of integrating these local models into global streamlines with similar diffusion profiles are really helpful to improve specificity and sensitivity respectively [4]. At the interface between these key methodological contributions, a large number of algorithms are available to extract WM fascicles, which inspired multiple efforts to evaluate the different approaches such as integrating appropriate phantoms as a common experimental dataset for comparison [5, 6]. Among these efforts, the DTI tractography challenge has sought since 2011 to evaluate CST reconstruction in presurgical planning of brain tumor extraction. The challenge resides in that quality of the data depends on patient cooperation and clinical stability and image processing must be quick. In this 4^{th} edition, 2 cooperative patients underwent a DW-MRI protocol at clinical isotropic spatial resolution of $2 \times 2 \times 2$ mm^3, which consisted of 69 diffusion sensitizing gradients (DSG) distributed on 4 different shells ($b = 200, 500, 1000, 3000$ s/mm^2). Data were sent to the participants for left and right CST reconstruction.

In this paper, we fitted, in each voxel independently, a white matter microstructure model coined Diffusion Directions Imaging (DDI) [7], that characterizes free water, intra- and extra-axonal spaces. We subsequently synthesized streamlines of the CST from these local microstructure models using a particle filter adapted to multi-modal distributions [8] initialized in a seeding region. We filtered the resulting streamlines by anatomical landmarks of the CST. A detailed description of the different steps involved in the reconstruction is provided in Section 2. In Section 3, we present our reconstructed CSTs. Evaluation is left to the organizers who designed specific comparative metrics.

2 From Diffusion-Weighted to Cortico-Spinal Imaging

2.1 Proposed processing pipeline

The following overall processing pipeline was used to extract the CST for the challenge datasets. It is a 4-step solution that pertains to:

1. *Non-Local Means (NLM) denoising.* We applied a Rician-adapted NLM filter [9] to the DW-MR images, which has been shown to efficiently reduce the amount of noise while preserving fine anatomical structures.
2. *Inference of local white matter microstructure models.* We designed a multi-compartment model of the white matter microstructure coined Diffusion Directions Imaging (DDI), which was inferred in each voxel from the denoised DW-MR images. Further details on this modeling and its inference are provided in Sections 2.4 and 2.5.

3. *Definition of regions of interest (ROI).* We delineated three ROIs based on state-of-the-art recommendations for picturing the CST with high specificity. Locations and extraction procedures are detailed in Section 2.7.
4. *Reconstruction of the left and right CST.* We depicted the left and right CST as multi-modal distributions of streamlines that were estimated from the local microstructure models using an enhanced particle filter, particularly suited for inferring multi-modal distributions like the CST. Further details are provided in Section 2.8.

All the tools used (NL-Means, WM microstructure estimator, tractography algorithm) were implemented utilizing ITK and VTK and are fully multi-threaded. We will distribute this diffusion toolbox as a free package soon.

2.2 Modeling the white matter microstructure

Different types of tissues are underlying an image of the brain. In the white matter for instance, the microstructure consists of axons, astrocytes, oligodendrocytes or microglia that might all populate a given voxel of the image, depending on the spatial resolution. These tissues can exhibit impermeable membranes, different shapes, axes of anisotropy, etc. All these features impose restrictions to the diffusion that ultimately yield different diffusion processes for each tissue type. As a result, the diffusion signal in a voxel conflates signals arising from each tissue type that populates the voxel. The voxelwise diffusion process is thus a finite mixture of single-tissue diffusion processes, which can be naturally characterized by a finite linear mixture model:

$$p_{\boldsymbol{X}}(\boldsymbol{x}; \pi_1, \ldots, \pi_C) = \sum_{i=1}^{C} \pi_i p_i(\boldsymbol{x}) \,, \tag{1}$$

where $\boldsymbol{X}$ is a random vector that describes voxelwise molecular displacements, $p_{\boldsymbol{X}}$ is its density which models the voxelwise diffusion process, C is the number of tissue types in the voxel. $\pi_1, \ldots, \pi_C$ and $p_1, \ldots, p_C$ are respectively the proportions and diffusion processes of each tissue type within the voxel. It can be related to the diffusion signal using the narrow pulse approximation [10].

$$S(b, \boldsymbol{g}) = B_0 \left|\varphi_{\boldsymbol{X}}(-b, \boldsymbol{g})\right| = B_0 \left|\sum_{i=1}^{C} \pi_i \varphi_i(-b, \boldsymbol{g})\right| \,, \tag{2}$$

where S is the noise-free diffusion signal observed for a diffusion-sensitizing gradient (DSG) of squared magnitude proportional to b (b-value) and direction $\boldsymbol{g}$, B_0 is the baseline signal in absence of DSG and φ denotes the characteristic function of a random variable. This yields a mathematical model for the diffusion signal that we coin Diffusion Compartment Imaging (DCI).

2.3 Modeling tissue-specific diffusion

We can further hypothesize a parametric distribution for single-tissue diffusion processes, which is very helpful for describing the diffusion signal in terms of microstructural parameters. Different propositions have been devised that mostly

pertain to the Gaussian distribution, from which (2) predicts mono-exponential diffusion signals in each tissue type. However, it has been recently shown that single-tissue non-Gaussian diffusion is more prevalent than expected [11, 12] and has been observed at high b-values [13]. We therefore model single-tissue diffusion with a non-Gaussian parametric DCI model that we recently introduced as Diffusion Directions Imaging (DDI). In general, it yields a non mono-exponential signal prediction, the analytic expression of which can be found in [7] and boils down to mono-exponential decay at low b-value regimes. The signal prediction depends on the following tissue-specific microstructural parameters:

- $\boldsymbol{\mu}_i \in \mathbb{S}^2$ represents the principal axis of diffusion;
- $\kappa_i \geq 0$ captures the concentration of molecular displacements around $\boldsymbol{\mu}_i$;
- $d_i > 0$ quantifies the amount of diffusion (diffusivity) occurring along $\boldsymbol{\mu}_i$;
- $\nu_i \in [0, 1]$ is the proportion of extra-axonal space within an axon bundle.

2.4 Parametric white matter microstructure model

We assume that a voxel is composed of M axon bundles, termed **fixels** [14], featuring different orientations. We explicitly add a mixture component p_0 in (1) to account for free water diffusion outside the fixels. Freely diffusing water is not subject to physical restrictions and thus undergo isotropic Gaussian diffusion, which is a particular case of our non-Gaussian distribution obtained for $\kappa_0 = 0$ and $\nu_0 = 0$. In addition, since we focus on white matter connectivity, the only source of free diffusion arises from CSF contamination for which $d_0 = 3 \times 10^{-3}$ mm^2/s [15], which leaves no free parameters for the isotropic component. This anisotropy needs to be maintained in the corresponding mixture components for interpreting them as fixels. We achieve this goal by setting the apparent diffusivities along and perpendicular to the fixel axis, termed **parallel** and **perpendicular** diffusivities, to the values of a typical white matter fixel. Such typical fixel can be characterized by fitting a single diffusion tensor to a set of low b-value images (typically less than 1500 s/mm^2) and averaging the tensors with high fractional anisotropy (e.g., higher than 0.8). In DDI, the parallel and perpendicular diffusivities can be analytically expressed in terms of the microstructural parameters and applying the above constraints leads to:

$$\nu_i = \frac{\kappa_i - \kappa^{\text{fixel}}}{(\kappa_i + 1)(\kappa^{\text{fixel}} + 3)\xi(\kappa_i) - \kappa^{\text{fixel}} - 1} \text{ and } d_i = \frac{d_{/\!/}^{\text{fixel}}}{1 - 2\nu_i\xi(\kappa_i)}\,, \quad \text{where} \quad \kappa^{\text{fixel}} = \frac{d_{/\!/}^{\text{fixel}}}{d_{\perp}^{\text{fixel}}} - 1 \text{ and } \xi(\kappa_i) = \frac{\coth\kappa_i}{\kappa_i} - \frac{1}{\kappa_i^2}\,. \tag{3}$$

The application of constraints (3) reduces the number of free parameters per fixel to 4, namely the polar and azimuthal angles $(\theta_i, \phi_i) \in [0, \pi] \times [0, 2\pi]$ that define the fixel axis $\boldsymbol{\mu}_i$, the concentration κ_i of molecular displacements around the fixel axis and the fraction of occupancy π_i of the fixel within the voxel. With M assumed fixel components and one isotropic diffusion component without free parameters, the total number of free microstructural parameters is $4M$.

2.5 Estimating the microstructure model in presence of noise

For a given DSG, we observe a noisy diffusion image, referred to as the **observed image**, and the multi-tissue microstructure model introduced in Section 2 predicts a noise-free diffusion image, referred to as the **predicted image**. We hypothesize that each observed image is corrupted by Gaussian noise centered on the predicted image with variance σ^2. Free microstructure parameters ($\{\mu_i, \kappa_i, \pi_i\}_{i=1,\dots,M}$) and nuisance parameters (B_0 and σ^2) are simultaneously estimated by maximizing their likelihood given the N observed images at different DSGs. The dimension of the optimization problem is thus $4M+2$. In practice, we use the BOBYQA derivative-free local optimizer [16] to solve the optimization problem. The derivatives of the log-likelihood with respect to the nuisance parameters are easily accessible and yield the following updating equations:

$$\widehat{B_0}^{(k+1)} = \frac{\sum_{i=1}^{N} \widehat{A_i}^{(k)} S_i}{\sum_{i=1}^{N} \left(\widehat{A_i}^{(k)}\right)^2} \quad \text{and} \quad \widehat{\sigma^2}^{(k+1)} = \frac{1}{N}\sum_{i=1}^{N}\left(S_i - \widehat{B_0}^{(k+1)}\widehat{A_i}^{(k)}\right)^2, \quad (4)$$

where $\widehat{B_0}^{(k+1)}$ and $\widehat{\sigma^2}^{(k+1)}$ are the estimates of B_0 and σ^2 at iteration $k+1$, S_i is the observed image for DSG $(b_i, \boldsymbol{g}_i)$ and $\widehat{A_i}^{(k)}$ is the corresponding signal prediction according to the microstructure model at iteration k. We use (4) at each iteration of the optimization algorithm to update the nuisance parameters. As BOBYQA is a local optimizer, it becomes very sensitive to the initialization as the model complexity increases. We thus carefully designed the initialization step. Diffusivity constraints (3) yield the following bounds for κ_i:

$$\kappa_{\min} = \kappa^{\text{fixel}} \text{ and } \kappa_{\max} = \xi^{-1}\left(\frac{1}{\kappa^{\text{fixel}}+3}\right). \quad (5)$$

from which good initial guesses are obtained by sampling uniformly the tight interval $[\kappa_{\min}, \kappa_{\max}]$. Also, it is likely that fixels should be the primary occupiers in white matter voxels and thus we found that a good initial guess for the fractions of occupancy π_i is $0.9/M$, which basically assumes that 90% of a white matter voxel is occupied by fixels. Finally, each initial fixel axis is initialized as the primary eigenvector of the following direction cosine matrix:

$$\text{DCM}_{\text{init}} = c_\ell \boldsymbol{e}_1\boldsymbol{e}_1^\top + (1-c_\ell)c_p(u\boldsymbol{e}_1\boldsymbol{e}_1^\top + (1-u)\boldsymbol{e}_2\boldsymbol{e}_2^\top) + (1-c_\ell)(1-c_p)\boldsymbol{r}\boldsymbol{r}^\top, \quad (6)$$

where c_ℓ and c_p are the linear and planar coefficients of the diffusion tensor [17], $\boldsymbol{e}_1$ and $\boldsymbol{e}_2$ are the first two eigenvectors of the diffusion tensor corresponding to the two largest eigenvalues and u and $\boldsymbol{r}$ are random values in $[0,1]$ and $\mathbb{S}^2$ respectively. In other words, an initial orientation will be close to the primary eigenvector of a prolate tensor, or to a random linear combination of the first two eigenvectors of an oblate tensor, or to a random orientation uniformly sampled on the sphere for a spherical tensor.

2.6 Determining the number of fixels per voxel

Since the number M of fixels in the mixture model is unknown and spatially varies, the model estimation procedure was repeated for different numbers M ranging from $M = 0$ to $M = 3$. We assessed each model performance by computing the following estimate of the Akaike information criterion [18]:

$$\mathrm{AICu}(M) = -2\ell + \frac{4N(2M+1)}{N-4M-3} + N\log\left(\frac{N}{N-4M}\right), \tag{7}$$

where ℓ is the log-likelihood of the diffusion model parameters ($4M$ in total) and noise parameters (B_0 and σ^2) given the data. This is an unbiased estimate of the AIC that is much less prone to overfitting than the original AIC estimate. We subsequently compute an estimate of Akaike's weights used to produce an averaged estimated model from the original models. The averaged model is finally simplified using modularity clustering [19]. It relies on the orientation similarity between fixel components to automatically determine the appropriate number of fixels to be accounted for in each voxel. A representative component is obtained by intra-cluster unweighted averaging, which summarizes each cluster in the final mixture model. The detailed equations and procedures required for DCI averaging can be found in [20, 21].

2.7 Identifying CST-specific anatomical landmarks

Anatomy of the CST An important component of obtaining the CST involves following the motor cortex fibers, which are somatotopically organized such that there is functional localization from the superior medial surface of the brain, where the foot is represented, moving laterally and anteroventrally to the Sylvian fissure, where head and face are represented. The somatotopic organization of the primary motor cortex (M1) was described by Penfield and Rasmussen [3].

M1 is comprised of the precentral gyrus (preCG), which extends anteriorly from the central sulcus to the precentral sulcus. At the apex of the brain the precentral gyrus (M1) and the postcentral gyrus (somatosensory cortex) fuse and form a paracentral lobule. Somatotopigraphically, the apical area of M1 represents the lower extremity and at the base of the sensorimotor strip, looking at a sagittal slice, it can be seen that the sensorimotor strip will fuse in the area adjacent to the Sylvian fissure [22, 23]. It has been reported that the biggest diameter of the preCG is found anteroventrally and inferiorly where the cortical representation of the lip and tongue have been described [23].

Other important anatomical landmarks for achieving high specificity in reconstructing the CST have been described. Specifically, [24, 25] suggest seeding the streamline generation on the superior-inferior radiations visible in the brainstem at the level of the decussating of the superior cerebellar peduncle (SCP) and filtering the output by keeping only those going through the superior-inferior radiations outlining the posterior limb of the internal capsule (PLIC).

ROI Delineation Based on these recommendations, we use a multiple region-of-interest (ROI) strategy to trace streamlines specific to the CST from the local microstructure information provided by the white matter microstructure models.

Specifically, SCP and PLIC were placed automatically as a local consensus region extracted from a collection of template ROI separately projected to the target diffusion tensor volume [26]. To do this, we independently projected 19 template ROI to the target image and then performed a consensus map analysis using the Simultaneous Truth and Performance Level Estimation (STAPLE) algorithm [27]. The underlying consensus for all of the projected templates consequently defines target-specific ROI which then are used for fiber tracking in the target diffusion tensor image.

The M1 ROI was delineated manually by a neuroanatomist expert (JMS). In MR imaging of clinical resolution at $2 \times 2 \times 2$ mm^3, partial volume effects may obscure the gyral-sulci boundary. In addition, it has been reported that boundary voxels and even voxels in the somatosensory cortex are also important to include in the ROI to fully produce the CST. As a result, we chose to delineate all these voxels to account for the contribution of low spatial resolution to incomplete tracing of the CST. In the present work, we included these voxels as part of M1.

2.8 Tracing the CST as a distribution of streamlines

We reconstructed the CST as a probability distribution of streamlines. We approximated this distribution using a particle filter with a multi-modal filtering distribution [8]. The particle filter approximates the distribution of streamlines as a collection of N weighted tracts (particles) of maximum length $L_{\max}$ all generated from the same seed point and clustered in an automatically determined number $C > C_{\min}$ of "super-tracts". Each tract grows sequentially by a step length ρ according to a 5-step procedure:

1. **Proposition of next direction.** Tracts are grown by sampling "outgoing" directions $\boldsymbol{v}^{(k+1)}$ according to the following proposal density:

$$q(\boldsymbol{v}^{(k+1)}; \boldsymbol{v}^{(k)}, \mathrm{DDI}) = \begin{cases} \displaystyle\sum_{i=1}^{M} \pi_i \mathcal{W}\left(\boldsymbol{v}^{(k+1)}; \boldsymbol{\mu}_i, \kappa_i^{\mathrm{DDI}}\right) & \text{if } M > 0, \\ \mathcal{W}\left(\boldsymbol{v}^{(k+1)}; \boldsymbol{v}^{(k)}, \kappa_{\mathrm{prior}}\right) & \text{if } M = 0, \end{cases} \tag{8}$$

   where $\boldsymbol{v}^{(k)}$ is the last incoming direction of the tract and $\mathcal{W}$ denotes the Watson distribution on the 2-sphere $\mathbb{S}^2$ [28]. The Watson distribution is a bipolar distribution centered on a mean axis with a given concentration around this axis. When the estimated local microstructure DDI model detects the presence of fixels ($M > 0$), the proposal is a mixture of Watson distributions centered on the fixel axes with concentration κ_i^{DDI} that depends on the microstructural parameters of each fixel. On the other hand, when no fixel is detected ($M = 0$), the proposal distribution is a single Watson distribution centered on the last incoming direction of the tract with a user-defined prior concentration κ_{prior}.

2. **Weight update after tract growth.** The weights of each grown tract are then updated by the ratio of the posterior distribution of the outgoing direction, given the local data (conformity to the data) over the proposal distribution. The posterior distribution of outgoing directions is obtained from Bayes theorem with a Gaussian likelihood on the diffusion signals and the prior distribution of (8) for $M = 0$.
3. **Resampling of the tract cloud.** Resampling is performed to avoid degeneration of weights when the effective sample size of each cluster drops below $\alpha\%$ of its actual sample size [29]. High-weight tracts are duplicated while low-weight ones are discarded.
4. **Checking stopping criteria.** A further advantage of using the DDI model is that stopping criteria can be based on microstrucural parameters rather than the non-specific FA. In details, we prevent growth of tracts which have reached voxels with free water fraction above π_0^{thr} or with extra-axonal proportion above ν_{thr} within all the fixel components. In other words, a tract is stopped either if the end voxel is almost exclusively outside the white matter or if all the fixels are too damaged.
5. **Tract clustering.** The proposed particle filter for tractography is an enhanced version of the traditional particle filter [30, 31] that better maintains the multi-modality of the distribution of tracts within the CST (multiple bifurcations can be thought as multiple modes of the distribution of tracts) by clustering tracts into "super-tracts" at each step. Clusters of "super-tracts" are redefined as follows: tracts are first merged pairwise if their Hausdorff distance is below H_{thr} and the resulting tracts are subsequently splitted in two if the directional homogeneity of the outgoing directions (characterized by the concentration of a von Mises & Fisher distribution [28]) is below κ_{split}.

3 Results

The 2014 MICCAI DTI tractography challenge consists of two patients suffering from tumors of various forms and grades. In addition to DWI, T1 and T2 weighted images were available along with the delineation of the tumors so that joint views of anatomical and tractography information could be created.

On both patients, the estimation of the local microstructure DDI models took 1 hour on a 32-core (16 physical cores) Xeon 2.7 GHz computer while the tractography of each CST took 20 minutes for $N = 5000$ initial particles (computation time proportional to N). The model estimation step is longer but still reasonably short and can be performed offline in a clinical context. The following parameters were used for the tractography algorithm: $N = 5000$, $L_{\max} = 15$ cm, $C_{\min} = 10$, $\rho = 1$ mm, $\kappa_{\text{prior}} = 20$, $\alpha = 50\%$, $\pi_0^{\text{thr}} = 0.6$, $\nu_{\text{thr}} = 0.6$, $H_{\text{thr}} = 0.5$ mm and $\kappa_{\text{split}} = 30$.

Figure 1 presents views of the left and right CST extracted on the first patient, superimposed on the T2w image. In addition, we superimposed the manual delineations of the tumor to provide 3D visualizations for evaluation of the relative positions of the tumor and motor pathways. Several remarks may be

expressed for patient 1. First, the left CST, not affected by the tumor, spreads into all the different motor cortex areas (see fig. 1a,b) thanks to the combination of the DDI model and our multi-modal probabilistic tractography. Secondly, the right CST is not going into the tumor region (fig. 1a,b) while still being able to depict correctly axonal bendings towards the face area and exhibits sparse tracts in the edema area (fig. 1a-c). This is due to the location of the tumor right next to the motor cortex area through which we filtered the generated streamlines, leaving many fewer streamlines on the right side with respect to the left side.

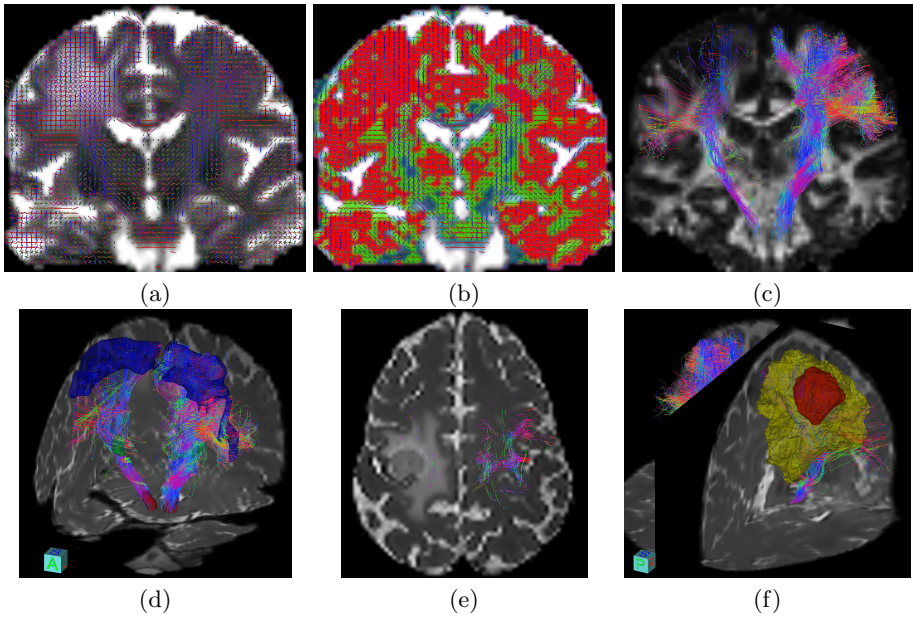

Fig. 1. Illustration of Patient 1's CST. (a,b): Estimated DDI models overlaid on the B0 and on the map of number of detected fixels (blue: 1, green: 2, red: 3). (c): left and right CST overlaid on the patient's FA image, (d): 3D view of the CST and seeding ROI utilized for tractography, (e,f): 3D and axial views of the CST together with the tumor (red: tumor, yellow: edema) highlighting their proximity.

Figure 2 presents results for patient 2. For this patient, the tumor has grown and pushed into the surrounding tissues, thereby shifting the CST. However, illustrations show that, although shifted, the tracts are still present on both sides of the brain. As a result, both CSTs (left and right) are well depicted by our tractography, while not going into the tumor area, which is located below. It may be noted that, surprisingly, more tracts are depicted on the left side where the tumor is located. However, this may be explained by two facts: (i) the tumor is not directly on the CST and (ii) since the whole left area was shifted, the

automatic PLIC ROI was manually corrected on the left side, which may have introduced an imbalance between the sizes of the left and right PLIC ROIs.

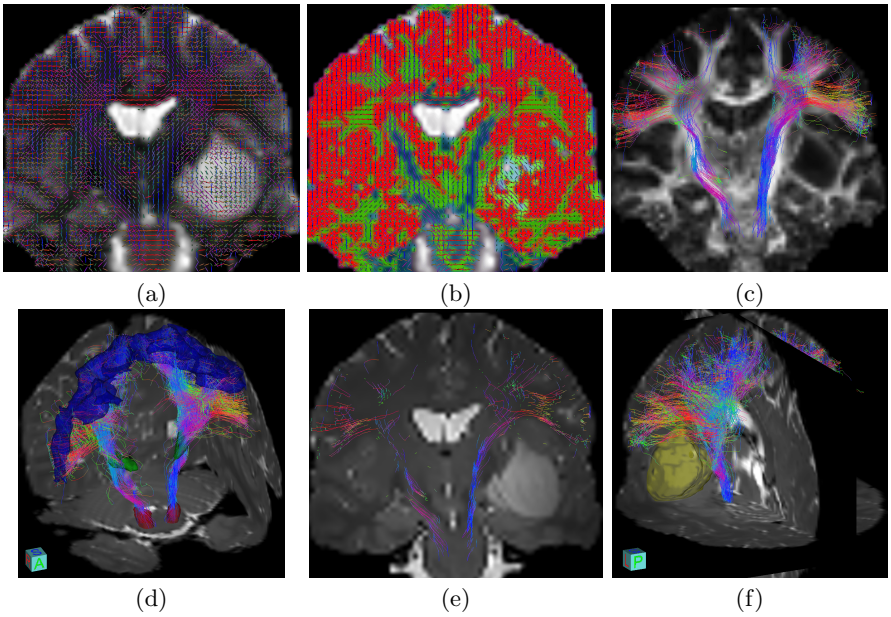

Fig. 2. Illustration of Patient 2's CST. (a,b): Estimated DDI models overlaid on the B0 and on the map of number of detected fixels (blue: 1, green: 2, red: 3). (c): left and right CST overlaid on the patient's FA image, (d): 3D view of the CST and seeding ROI utilized for tractography, (e,f): 3D and axial views of the CST together with the tumor (red: tumor, yellow: edema) highlighting their proximity.

Finally, both figures also present the estimated models, demonstrating their capability to resolve intricate fixel configurations (e.g., in the semioval centrum). These figures also demonstrate how the CST information may be fused with the tumor delineations and other modalities to help in understanding how the tumor affects the CST and ultimately in presurgical planning of brain tumor extraction.

4 Perspectives

Our pipeline was able to provide an accurate reconstruction of the CST for both patients along with a visualization that we think could be helpful to the neurosurgeon. It seems that we were able to reach all areas of the motor cortex. However, several steps involved in the CST reconstruction could be further improved. The following points are currently under investigation:

– Noise in DW-MRI is not Gaussian and a better noise model could yield a better inference of the local white matter microstructure models;

- The clustering of the particle cloud in the tractography algorithm is very simple and dichotomous. More efficient and continuous clustering strategies can help in even better maintaining the axonal bendings;
- Pertaining to the CST, the boundaries of the motor cortex are unclear and the literature suggests it might be dependent on the spatial resolution. To test the contribution of different segments of M1 and surrounding areas to the full reconstruction of the CST, a series of labels were used to demarcate these areas and we are currently testing the optimality and reproducibility of particular areas for tractography of the CST.

Acknowlegment This investigation was supported by NIH Grant R01 LM010033.

References

1. Le Bihan, D.: Looking into the functional architecture of the brain with diffusion MRI. Nature Rev. Neurosci. **4**(6) (2003) 469–80
2. Jellison, B.J., Field, A.S., Medow, J., Lazar, M., Salamat, M.S., Alexander, A.L.: Diffusion tensor imaging of cerebral white matter: a pictorial review of physics, fiber tract anatomy, and tumor imaging patterns. Am. J. Neurorad. **25**(3) (2004) 356–69
3. Penfield, W., Rasmussen, T.: The cerebral cortex in man. Macmillan (1950)
4. Behrens, T., Johansen-Berg, H., Jbabdi, S., Rushworth, M., Woolrich, M.: Probabilistic diffusion tractography with multiple fibre orientations: What can we gain? NeuroImage **34**(1) (2007) 144–55
5. Fillard, P., Descoteaux, M., Goh, A., Gouttard, S., Jeurissen, B., Malcolm, J., Ramirez-Manzanares, A., Reisert, M., Sakaie, K., Tensaouti, F., Yo, T., Mangin, J.F., Poupon, C.: Quantitative evaluation of 10 tractography algorithms on a realistic diffusion MR phantom. NeuroImage **56**(1) (2011) 220–234
6. Côté, M., Boré, A., Girard, G., Houde, J., M., D.: Tractometer: online evaluation system for tractography. In: MICCAI. (2012) 699–706
7. Stamm, A., Pérez, P., Barillot, C.: A new multi-fiber model for low angular resolution diffusion MRI. In: Proc. I. S. Biomed. Imaging, IEEE (2012) 936–939
8. Stamm, A., Commowick, O., Barillot, C., Pérez, P.: An adaptive multi-modal particle filter for white matter probabilistic tractography. In: Inf. Process. Med. Imaging, Springer LNCS 7917 (2013) 594–606
9. Wiest-Daesslé, N., Prima, S., Coupé, P., Morrissey, S.P., Barillot, C.: Rician noise removal by non-local means filtering for low signal-to-noise ratio MRI: applications to DT-MRI. In: MICCAI, Springer (2008) 171–9
10. Callaghan, P.: Principles of Nuclear Magnetic Resonance microscopy. Oxford University Press (1991)
11. Yoshiura, T., Wu, O., Zaheer, A., Reese, T.G., Sorensen, A.G.: Highly diffusion-sensitized MRI of brain: dissociation of gray and white matter. Magn. Reson. Med. **45**(5) (2001) 734–40
12. Wang, B., Kuo, J., Bae, S., Granick, S.: When Brownian diffusion is not Gaussian. Nat. Mater. **11**(6) (June 2012) 481–5
13. De Santis, S., Gabrielli, A., Palombo, M., Maraviglia, B., Capuani, S.: Non-Gaussian diffusion imaging: a brief practical review. Magn. Reson. Imaging **29**(10) (December 2011) 1410–6

14. Raffelt, D., Smith, R., Tournier, J., Vaughan, D., Jackson, G., Connelly, A.: Fixel-Based Morphometry: Whole-Brain White Matter Morphometry in the Presence of Crossing Fibres. In: ISMRM. Volume 22., Milan (Italy) (2014) 22:0731
15. Caan, M.W.a., Khedoe, H.G., Poot, D.H.J., den Dekker, A.J., Olabarriaga, S.D., Grimbergen, K.a., van Vliet, L.J., Vos, F.M.: Estimation of diffusion properties in crossing fiber bundles. IEEE Trans. Med. Imaging **29**(8) (August 2010) 1504–15
16. Powell, M.: The BOBYQA algorithm for bound constrained optimization without derivatives. Technical report, Centre for Mathematical Sciences, University of Cambridge, UK (2009)
17. Westin, C.F., Maier, S.E., Mamata, H., Nabavi, A., Jolesz, F.a., Kikinis, R.: Processing and visualization for diffusion tensor MRI. Med. Image Anal. **6**(2) (June 2002) 93–108
18. McQuarrie, A., Shumway, R., Tsai, C.: The model selection criterion AICu. Stat. Probab. Lett. **34**(3) (June 1997) 285–292
19. Newman, M.E.J.: Modularity and community structure in networks. Proc. Natl. Acad. Sci. U. S. A. **103**(23) (June 2006) 8577–82
20. Stamm, A., Commowick, O., Pérez, P., Barillot, C.: Fast identification of optimal fascicle configurations from standard clinical diffusion MRI using Akaike information criterion. In: 2014 11th IEEE Int. Symp. Biomed. Imaging. Number Mcm, Beijing (China) (2014) 238–241
21. Stamm, A., Scherrer, B., Commowick, O., Barillot, C., Warfield, S.: Fast and robust detection of the optimal number of fascicles in diffusion images using model averaging theory. In: ISMRM. Volume 22., Milan (Italy) (2014) 22:2629
22. Ebeling, U., Huber, P., Reulen, H.: Localization of the precentral gyrus in the computed tomogram and its clinical application. J Neurol **233**(2) (1986) 73–76
23. Ono, M., Kubik, S., Abernathey, C.: Atlas of the cerebral sulci. Georg Thieme (1990)
24. Wakana, S., Caprihan, A., Panzenboeck, M.M., Fallon, J.H., Perry, M., Gollub, R.L., Hua, K., Zhang, J., Jiang, H., Dubey, P., et al.: Reproducibility of quantitative tractography methods applied to cerebral white matter. Neuroimage **36**(3) (2007) 630–644
25. Zhang, Y., Zhang, J., Oishi, K., Faria, A.V., Jiang, H., Li, X., Akhter, K., Rosa-Neto, P., Pike, G.B., Evans, A., et al.: Atlas-guided tract reconstruction for automated and comprehensive examination of the white matter anatomy. Neuroimage **52**(4) (2010) 1289–1301
26. Suarez, O., R., Commowick, O., Prabhu, P., S., Warfield, K., S.: Automated delineation of white matter fiber tracts with a multiple region-of-interest approach. Neuroimage **59**(4) (February 2012) 3690–3700
27. Commowick, O., Akhondi-Asl, A., Warfield, K., S.: Estimating A Reference Standard Segmentation with Spatially Varying Performance Parameters: Local MAP STAPLE. IEEE Transactions on Medical Imaging **31**(8) (2012) 1593–1606
28. Jupp, P., Mardia, K.: A unified view of the theory of directional statistics. Int. Stat. Rev. **57**(3) (1989) 261–294
29. Doucet, A., Godsill, S., Andrieu, C.: On sequential Monte Carlo sampling methods for Bayesian filtering. Stat. Comput. **10**(3) (2000) 197–208
30. Zhang, F., Hancock, E.R., Goodlett, C., Gerig, G.: Probabilistic white matter fiber tracking using particle filtering and von Mises-Fisher sampling. Med. Image Anal. **13**(1) (2009) 5–18
31. Pontabry, J., Rousseau, F., Oubel, E., Studholme, C., Koob, M., Dietemann, J.L.: Probabilistic Tractography Using Q-Ball Imaging and Particle Filtering: Application to Adult and in-utero Fetal Brain Studies. Med. Image Anal. (2012)